ADVANCED FUNCTIONAL MATERIALS
www.afm-journal.de

Osteoconductive Performance of Carbon Nanotube Scaffolds Homogeneously Mineralized by Flow-Through Electrodeposition

Stefania Nardecchia, M. Concepción Serrano, María C. Gutiérrez, M. Teresa Portolés, M. Luisa Ferrer,* and Francisco del Monte*

The treatment of bone lesions, including fractures, tumor resection and osteoporosis, is a common clinical practice where bone healing and repair are pursued. It is widely accepted that calcium phosphate-based materials improve integration of biomaterials with surrounding bone tissue and further serve as a template for proper function of bone-forming cells. Within this context, mineralization on preformed substrates appears as an interesting and successful alternative for mineral surface functionalization. However, mineralization of "true" 3D scaffolds –in which the magnitude of the third dimension is within the same scale as the other two– is by no means a trivial issue because of the difficulty to obtain a homogeneous mineral layer deposited on the entire internal surface of the scaffold. Herein, a "flow-through" electrodeposition process is applied for mineralization of 3D scaffolds composed of multiwall carbon nanotubes and chitosan. It is demonstrated that, irrespective of the experimental conditions used for electrodeposition (e.g., time, temperature and voltages), the continuous feed of salts provided by the use of a flow-through configuration is the main issue if one desires to coat the entire internal structure of 3D scaffolds with a homogeneous mineral layer. Finally, mineralized scaffolds not only showed a remarkable biocompatibility when tested with human osteoblast cells, but also enhanced osteoblast terminal differentiation (as early as 7 days in calcifying media).

1. Introduction

The treatment of bone lesions, including fractures, tumor resection and osteoporosis, is a common clinical practice where bone healing and repair are pursued. Over 6.2 million bone fractures occur in the U.S.A. per year and approximately 10% fail to heal properly.[1] Moreover, 10 million people are currently affected by osteoporosis, with sanitary costs of billions of dollars and a significant increase estimated for the next decades.[2] To treat these pathologic conditions, about 2.2 million bone graft procedures are performed annually in the world.[3] Even when autologous bone grafts remain as the gold standard for this type of interventions, limited supply and donor site morbidity are significant limitations for this practice. Within this context, bone tissue engineering has arisen as an alternative technology for the fabrication of substitutes that functionally fill bone tissue defects while promoting adequate healing. As hydroxyapatite is the main mineral component of native bone, most efforts in the field have been directed toward the development of materials containing hydroxyapatite or related calcium phosphates.[4–6] It has been extensively demonstrated that calcium phosphate-based materials improve integration of biomaterials with surrounding bone tissue and further serve as a template for proper function of bone-forming cells. Although significant challenges still remain when creating substitutes for bone tissue,[7] biomimetic approaches are currently gaining much attention.[8]

S. Nardecchia
Instituto de Ciencia de Materiales de Madrid (ICMM)
Consejo Superior de Investigaciones Científicas (CSIC)
Campus de Cantoblanco, 28049-Madrid, Spain

Dr. M. C. Serrano
Instituto de Ciencia de Materiales de Madrid (ICMM)
Consejo Superior de Investigaciones Científicas (CSIC)
Campus de Cantoblanco, 28049-Madrid, Spain
E-mail: conchi.serrano@icmm.csic.es

Dr. M. C. Gutiérrez
Instituto de Ciencia de Materiales de Madrid (ICMM)
Consejo Superior de Investigaciones Científicas (CSIC)
Campus de Cantoblanco, 28049-Madrid, Spain

Dr. M. T. Portolés
Department of Biochemistry and Molecular Biology I
Universidad Complutense de Madrid
28040-Madrid, Spain

Dr. M. L. Ferrer
Instituto de Ciencia de Materiales de Madrid (ICMM)
Consejo Superior de Investigaciones Científicas (CSIC)
Campus de Cantoblanco, 28049-Madrid, Spain
E-mail: mferrer@icmm.csic.es

Dr. F. del Monte
Instituto de Ciencia de Materiales de Madrid (ICMM)
Consejo Superior de Investigaciones Científicas (CSIC)
Campus de Cantoblanco, 28049-Madrid, Spain

DOI: 10.1002/adfm.201200684

Despite the complex interactions at the biomacromolecule-mineral nucleus interface that govern mineralization processes are yet incompletely understood, it is generally assumed that nucleation initiates at such interface.[9–13] Thus, the most common approach for fabricating organic-inorganic composites is crystal morphogenesis in polymer-containing solutions that are subsequently processed into the required structure (by electrospinning or freeze-casting, among others).[14–22] The main limitations of this strategy come from, first, the reduced mineral content that can be typically incorporated into the composite and, second but principal, the occlusion of the mineral within the polymer matrix that impedes its interaction with cells. This latter issue is particularly undesired, as it will ultimately limit the potential functionality provided by the presence of mineral components. Mineralization on preformed substrates appears as an interesting and successful alternative for mineral surface functionalization.[23–27] The excellent control of the mineralized layer in terms of both thickness and homogeneity makes this approach particularly attractive to coat two-dimensional substrates with independence of their chemical composition. However, the achievement of a homogeneous layer of mineral deposited on the internal surface of "true" three-dimensional (3D) scaffolds (in which the magnitude of the third dimension is within the same scale as the other two) is a challenge because the diffusion of any type of matter throughout the 3D structure is restricted.[28] Under these circumstances, crystal growth can be faster than the replenishment of salts so that large crystals grow at the expense of small ones in an Ostwald ripening-like process.[27]

Recently, electrodeposition has been proposed as an alternative to accelerate mineralization processes. This technique has been extensively used to obtain apatite coatings on a number of substrates, the nature of which ranged from metallic (e.g. stainless steel, titanium and their alloys) to non-conductive (e.g., TiO_2 or polymers).[29–34] Hydroxyapatite mineralization has been also achieved on carbon nanotube polymer composites in which concerns about biocompatibility were addressed by studying not only simple cellular processes such as adhesion and proliferation,[35,36] but also more relevant phenomena for bone formation such as osteoblast differentiation.[8,37,38] All these examples reveal the success of electrodeposition techniques for mineralization of 2D substrates and even 3D scaffolds in which the third dimension was around a few hundreds of micrometers.[39] However, the successful application of these techniques for mineralizing the internal structure of "true" 3D scaffolds is yet challenging because the restrictions mentioned above for regular mineralizations[27] also apply in this case.[34]

Herein, we have applied electrodeposition techniques to obtain a homogenous coating of different calcium phosphate crystals onto the internal structure of 3D scaffolds composed of multiwall carbon nanotubes (MWCNT) and chitosan (CHI). The scaffolds were obtained by the application of the ISISA process (ice segregation induced self-assembly)[40–44] to an acid aqueous solution of CHI where MWCNT were also suspended.[45] In these scaffolds, MWCNT acted as bricks providing not only structural but also conductive properties, while the organic biocompatible component CHI acted as mortar contributing to the reinforcement of the structure. These and other carbon nanotube-based scaffolds have already proved efficacy as filters and catalyst support membranes,[46] vapor and pressure sensors,[47] fluorescent aerogels,[48] conductive scaffolds,[49,50] and scaffolds for bone tissue regeneration,[51] among others. In this work, we benefited from their capability as electrodes and biomaterials. The scaffolds were exposed to glutaraldehyde vapors prior electrodeposition experiments because, otherwise, the scaffold structure would collapse upon dissolution of CHI in the acid aqueous solution of calcium and phosphate salts that was used for mineralization.[27] Electrodeposition experiments were carried out in both static and "flow-through" configuration. X-ray and selected area electron diffraction (XRD and SAED, respectively) were used to determine the nature of the deposit. Whether the deposit was homogeneously coating the entire internal structure of the 3D scaffolds was investigated by scanning electron microscopy (SEM). Finally, the behavior of human Saos-2 osteoblasts when cultured on mineralized scaffolds was explored in order to evaluate the potential applicability of these materials as osteoconductive matrices for bone healing and regeneration.

2. Results and Discussion

NTC scaffolds (where NT stands for multiwall carbon nanotubes and C for chitosan) were prepared by the ISISA process, which basically consists of the unidirectional freezing of the acid aqueous solution of CHI, in which MWCNT were also suspended, and its subsequent freeze-drying. The application of this unidirectional freezing is critical for the achievement of microchanneled-type longitudinal structures (**Figure 1**).[22,40,52–54] NTCG scaffolds (additional G stands for glutaraldehyde) were obtained upon CHI crosslinking by diffusion of glutaraldehyde vapors throughout the scaffold microchannels. As compared to NTC scaffolds, neither the conductive properties nor the morphology of NTCG scaffolds experienced significant modifications by this treatment (see Supporting Information (SI): Figure 1-SI and Table 1-SI), and it allowed for the preservation of the peculiar 3D structure of these scaffolds after soaking into the acid aqueous medium that contains the calcium and phosphate salts used for mineralization.[27]

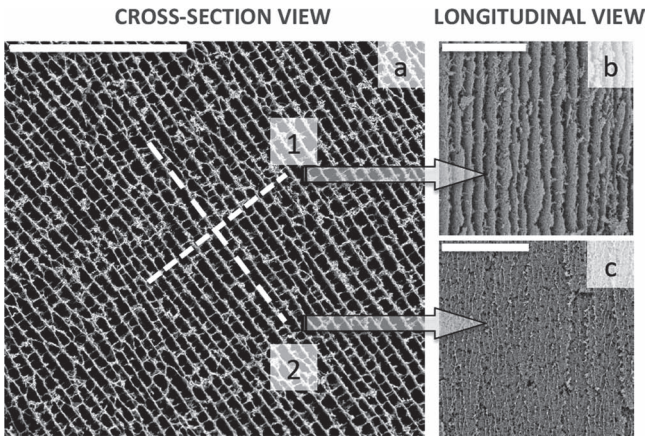

Figure 1. SEM micrographs of NTC scaffolds: (a) cross-section view, (b) longitudinal view according to plane 1 and (c) longitudinal view according to plane 2. Scale bars represent 200 μm in every case.

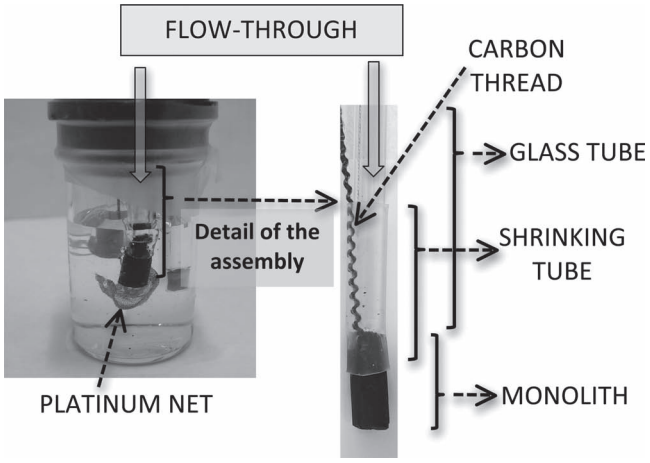

Figure 2. Scheme illustrating the set-up used for electrodeposition and the assembly of the NTCG scaffold that allows the electrolyte to flow through the microchanneled structure (by sealing the scaffold to the glass tube with the shrinking tube) and the application of the voltage required for electrodeposition (by using a carbon thread as current collector connected to the scaffold with the shrinking tube).

Despite the full mechanism governing mineralization is not yet fully understood, it is generally accepted that the electrochemical reactions result in a local increase of the pH at the vicinity of the cathode. As a consequence, supersaturation of calcium phosphate salts occurs and different calcium phosphates –including hydroxyapatite (HA), octacalcium phosphate (OCP) and dicalcium phosphate dihydrate (DCPD)– can be deposited onto the cathode surface.

In our case, electrodeposition was carried out under potentiostatic conditions in a three-electrode electrochemical system/cell in which one cylindrical NTCG scaffold (4.5 mm in diameter, 12 mm in height) was used as the working electrode and a platinum mesh as the counter electrode (**Figure 2**). First electrodeposition experiments were carried out over 30 min at 30 °C and 1.4 V. In non-flow conditions, SEM micrographs revealed that the presence of mineral clusters covering homogeneously the internal surface of the scaffold strictly depended on how far this surface was from the outer part of the monolith. Thus, mineral clusters were observed when we focused at an internal surface that was few microns in depth from the periphery of the cylinder, while a mineral cluster-depleted structure was observed further inwards the internal part of the monolith (Figure 2-SI). This radial heterogeneous structure was not observed when electrodeposition was carried out in the flow-through configuration. In this case, the homogeneous layer of clusters was extended throughout the entire internal structure. **Figure 3** shows a cross-section view of a NTCGM scaffold (additional M stands for mineralized) in which a homogeneous mineral layer covers a surface of ca. 0.9 mm × 0.9 mm that extends from the periphery inwards the centre of the cylinder. Interestingly, the homogeneous coating of the internal sample structure was also observed along the whole length of the cylinder used for electrodeposition as revealed in **Figure 4**. The capability to obtain homogeneous coatings for electrodepositions carried out over extended times and/or using different temperatures and voltages confirms that homogeneity is governed by the continuous feed of salts provided by the use of a flow-through configuration (**Figure 5**). It is worth noting that this methodology could be extended to other materials as far as they keep a microchanneled structure (to work in flow-through configuration) and retain certain conductivity (to apply the voltage required for electrodeposition).

The crystalline nature of the deposited mineral changed depending on the experimental conditions used for electrodeposition, so we decided to study this issue by XRD (**Figure 6**). In every case, XRD exhibited the main characteristic peaks for CNT at $2\theta = 26.5°$ and $54.3°$.[27] The XRD pattern of the mineral coating electrodeposited over 30 min at 30 °C and 1.4 V exhibited a peak at $2\theta = 11.7°$ that, according to the JCPDS

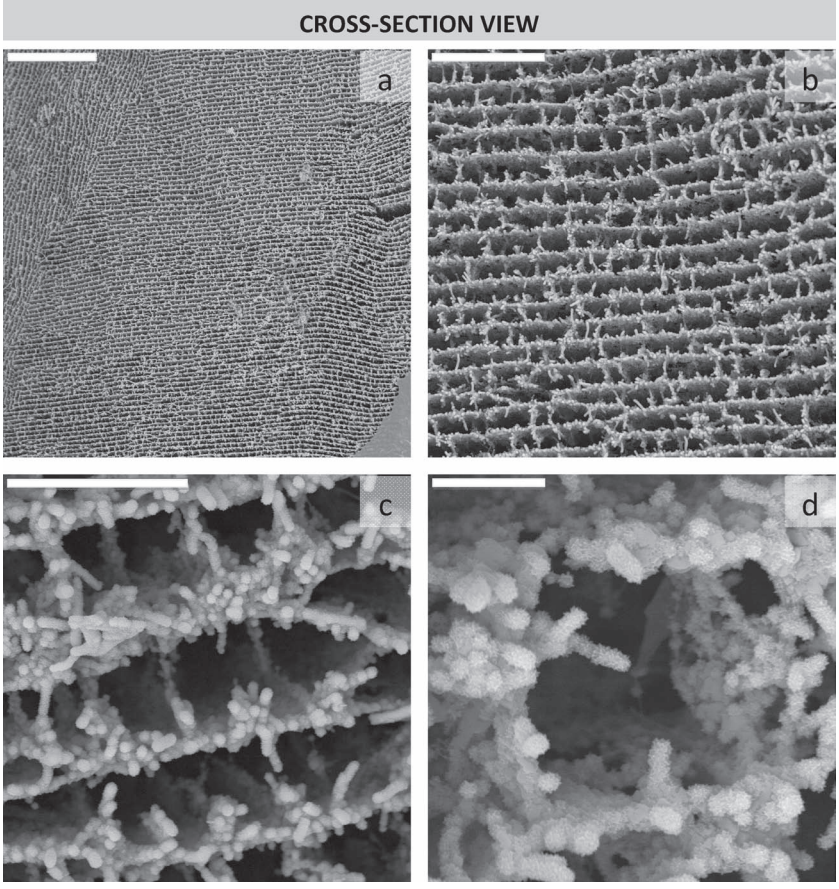

Figure 3. SEM micrographs of NTCGM scaffolds after mineralization in flow-through conditions revealing the long-range homogeneity of the mineral coating across the entire scaffold structure. Electrodeposition was carried out over 30 min at 30 °C and 1.4 V. Scale bars represent 200 μm (a), 50 μm (b), 20 μm (c), and 5 μm (d).

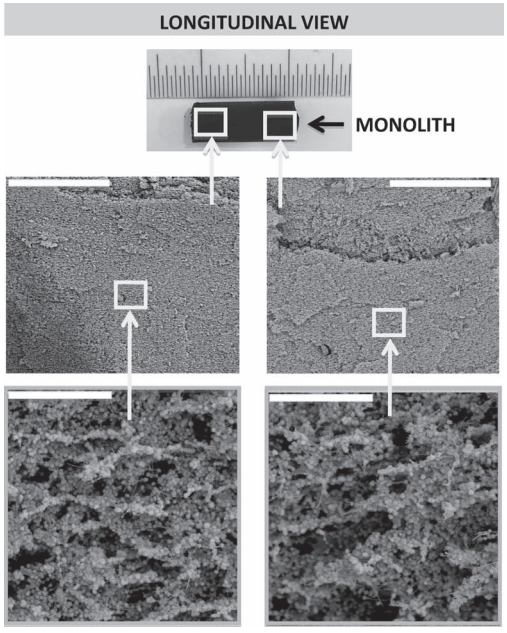

Figure 4. SEM micrographs of NTCGM scaffolds after mineralization in flow-through conditions revealing the long-range homogeneity of the mineral coating along the entire scaffold structure of the monolith. Electrodeposition was carried out over 30 min at 30 °C and 1.4 V. Scale bars represent 400 µm (top) and 20 µm (bottom).

card (Joint Committee on Powder Diffraction Standards), corresponded to DCPD (card number 09-0077) (Figure 6a). The selected area electron diffraction (SAED) pattern performed in TEM for DCPD crystals was also consistent with the XRD pattern and reflections belonging to (020), (021), (041), (221), and (220) planes were observed respectively at d_{020} = 0.771 nm, d_{021} = 0.399 nm, d_{041} = 0.306 nm, d_{221} = 0.289 nm, and d_{220} = 0.254 nm in **Figure 7**a. We also investigated the mineralized coating when electrodeposition was performed over 30 min at 60 °C (rather than 30 °C) and 1.4 V (Figure 6b). The XRD pattern exhibited two peaks (at 2θ = 9.4° and 4.7°, the latter very intense) that corresponded to OCP (card number 26-1056). The peaks ascribed to OCP were also observed when electrodeposition was extended over 180 min at 30 °C and 1.4 V (Figure 6a), albeit their intensity was lower than that observed in the previous case. In this case (e.g. 30 °C – 180 min – 1.4 V), the intensity of the group of peaks centred at 2θ = 31.7° also exhibited a certain increase that revealed the appearance of HA (card number 09-0432) as a minor component. The intensity of the peaks ascribed to OCP (at 2θ = 9.4° and 4.7°) also decreased when mineralization was prolonged over time up to 180 min at 60 °C and 1.4 V, whereas the intensity increase of the peak at 2θ = 31.7° confirmed the major presence of HA (Figure 6b). Interestingly, the increase of the voltage from 1.4 to 1.8 up to 2.1 V also provided the transition from DCPD to HA via OCP as intermediate for electrodepositions carried out at 30 °C over 30 min (Figure 6a), whereas at 60 °C (and over 30 min) OCP was the major phase observed at every voltage (Figure 6b). It was worth noting that the proper selection of the experimental conditions used for electrodeposition provided highly pure crystalline phases of DCPD, OCP and HA (e.g. 30 °C – 30 min – 1.4 V, 60 °C – 30 min – 1.4 V and 30 °C – 30 min – 2.1 V, respectively).

SEM and TEM micrographs showed that the morphology of the crystallites forming these coatings was consistent with the different crystalline phases observed at the XRD patterns (Figure 3, 4, 5, and 7). Thus, DCPD crystals obtained upon electrodeposition over 30 min at 30 °C and 1.4 V exhibited a flower-like morphology consisting of small interlocking individual platelets (Figure 3d and 7b). Meanwhile, the OCP crystals obtained upon electrodeposition over 30 min at 60 °C and 1.4 V showed a sharp edge plate-like morphology in which the platelets were larger than those of DCPD crystals and exhibited either large flower-like organizations (Figure 5d) or no organization (Figure 5b, 5c and 7c). Finally, the morphology of HA crystals obtained upon electrodeposition over 180 min at 60 °C and 1.4 V was needle-like (Figure 7d), whose aggregation around

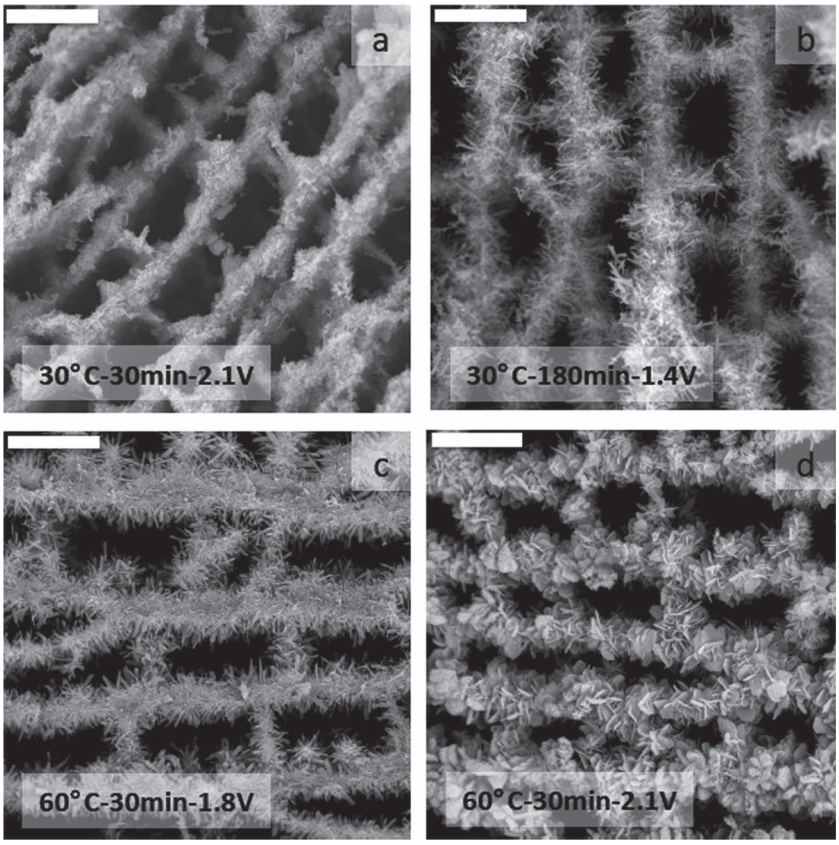

Figure 5. SEM micrographs of NTCGM scaffolds after mineralization in flow-through conditions that reveal the homogeneity of the mineral coating irrespective of the experimental conditions used for electrodeposition; (a) 30 °C – 30 min – 2.1 V, (b) 30 °C – 180 min – 1.4 V, (c) 60 °C – 30 min – 1.8 V, and (d) 60 °C – 30 min – 2.1 V. Scale bars represent 20 µm in every case.

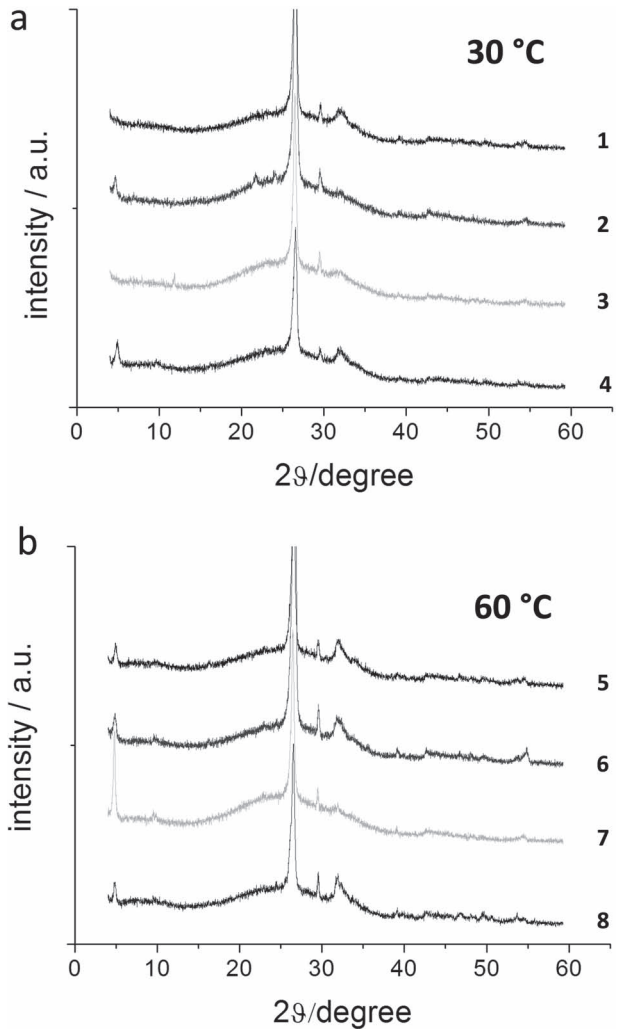

Figure 6. XRD patterns of NTCGM scaffolds after mineralization in flow-through conditions and using different experimental conditions for electrodeposition: (a)30 °C over 30 min at 2.1 V (1), 1.8 V (2), and 1.4 V (3); and 30 °C over 180 min at 1.4 V (4) and (b)60 °C over 30 min at 2.1 V (5), 1.8 V (6), and 1.4 V (7); and 60 °C over 180 min at 1.4 V (8).

the MWCNT provided a pseudo-amorphous resemblance to the resulting clusters (Figure 5a). In this latter case, crystals resembling OCP morphology were also observed by TEM in agreement with the above-discussed XRD. Energy dispersive X-ray (EDX) analyses were also performed in TEM for these three samples. The Ca:P ratio found for DCPD, OCP and HA were ca. 1.11, 1.27 and 1.45, in agreement with the theoretical ones (1.0, 1.33 and 1.66 considering that their molecular formula is $CaHPO_4 \cdot 2H_2O$, $Ca_8H_2(PO_4)_6 \cdot 5H_2O$ and $Ca_{10}(PO_4)_6(OH)_2$, respectively). The particularly low Ca:P ratio found for HA could be ascribed to the presence of some remaining OCP[55] that, as observed by XRD, was not yet fully converted into HA in the particular conditions used for electrodeposition (at 60 °C and 1.4 V over 180 min).

Both DCPD and OCP are considered precursor phases of HA. In particular, OCP has been postulated as the precursor phase of biological apatite in bone and teeth.[56] It is generally assumed that transition from DCPD to OCP up to HA occurs upon the rise of the pH from acidic to alkaline. In electrodeposition, the local increase of the pH that occurs at the vicinity of the cathode is responsible for supersaturation and hence, mineral precipitation. As described above, supersaturation conditions can be reached upon the rising of both the temperature and the voltage, and upon extending the mineralization process over time. In this work, we have demonstrated the capability to control the formation of highly pure phases of either DCPD, OCP or HA, which makes electrodeposition an easy tool for the preparation of different mineralized scaffolds. Considering that both DCPD and OCP are HA precursors, and HA itself can improve integration of biomaterials with surrounding bone tissue, we studied next the behavior of human Saos-2 osteoblasts when cultured on these scaffolds. As mentioned above, electrodeposition in flow-through conditions provided a homogeneous mineral coating throughout the entire internal structure of every scaffold irrespective of the crystalline phase of the deposited mineral. Nonetheless, we decided to use the scaffold mineralized with DCPD crystals (30 ºC – 30 min – 1.4 V) because of some particularly attractive features provided by the small size of these crystals (smaller than those of both OCP and HA). For instance, more surface area can be coated with small crystals because they can be packaged more tightly than the larger ones. Moreover, the roughness of the coating obtained from DCPD is also better suited for cell growth –in terms of formation of confluent cultures– than that from either OCP or HA.

Cell cultures were performed on disks of 4.5 mm in diameter and ca. 3 mm in height that were obtained by simple cryo-fracture of the electrodeposited scaffold (4.5 mm in diameter and 12 mm in height). Thus, we were able to obtain up to four disks from each NTCGM scaffold thanks to the homogeneity of the mineral coating that covers the entire internal structure. First cell studies focused on biocompatibility assessment, which constitutes an essential preliminary step in the evaluation of biomaterials with envisioned biomedical applications.[57] With the aim of investigating biomaterial interaction with human osteoblasts, cell adhesion was explored on NTCGM and NTC scaffolds (**Figure 8**). In agreement with previous results,[27,45] appropriate cell attachment and spreading was observed by scanning electron microscopy (SEM) in NTC and NTCGM scaffolds. Interestingly, cells tended to colonize the 3D scaffold structure by penetrating into the microchannels when the pore size was bigger than cell dimensions. We further explored if this appropriate cellular adhesion was accompanied by preservation of cell viability by using a live/dead staining. Thus, cells were observed on the scaffolds by confocal laser scanning microscopy (CLSM) confirming high-density cultures with a majority of cells being alive (**Figure 9**). As previously observed by SEM, cells colonized the material surface by accommodating the scaffold structure. Certain cell penetration in the microchannels was also observed. Unfortunately, the absence of a continuous flow guaranteeing the supply of nutrients and oxygen to internalized cells led to cell death in depths over several tens of microns. Further experiments under flow are currently being performed to benefit cell survival when colonizing the interior structure of the scaffolds. When quantified, a significant reduction in cell viability was observed in cultures on NTCG scaffolds as compared to

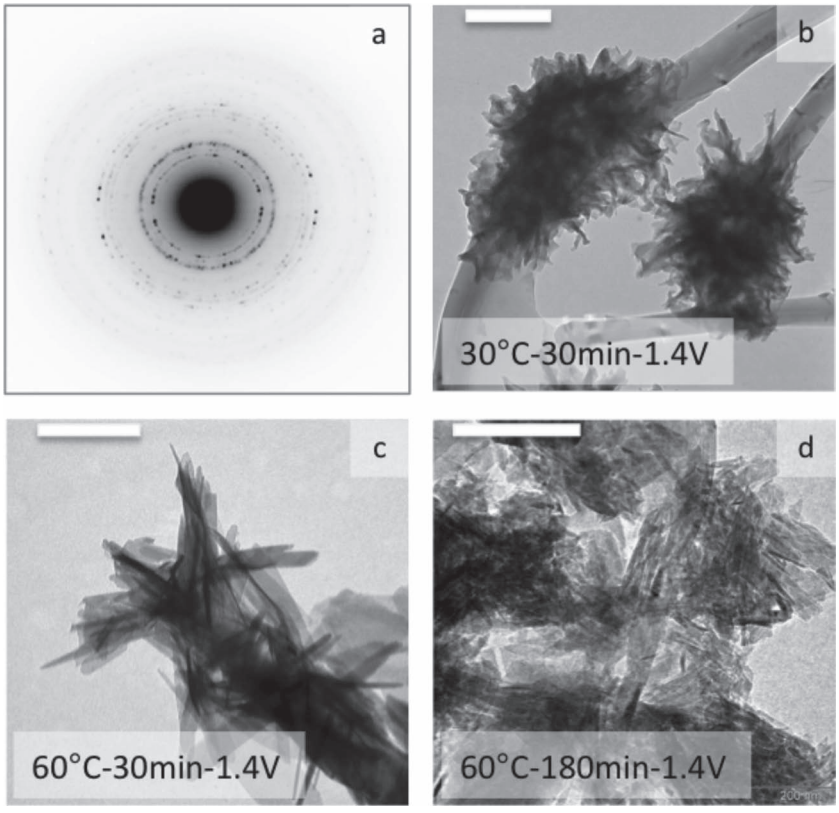

Figure 7. SAED in TEM of NTCGM scaffolds after mineralization in flow-through conditions over 30 min at 30 °C and 1.4 V (a). TEM micrographs revealing the different morphology of the deposited crystals depending on the experimental conditions used for electrodeposition: (b) 30 °C – 30 min – 1.4 V, (c) 60 °C – 30 min – 1.4 V, and (d) 60 °C – 180 min – 1.4 V. Scale bars represent 300 nm in every case.

NTC (77 ± 5.9% *vs.* 91 ± 1.3%, p = 0.000) (Table 2-SI). The presence of toxic residues of glutaraldehyde used for crosslinking has been proposed as the most plausible explanation for this result.[27] Interestingly, this harmful effect vanished in NTCGM scaffolds because of the DCPD coating and cell viability was recovered to the levels found in NTC scaffolds (85 ± 4.9% *vs.* 91 ± 1.3%, p = 0.063).

Once adequate biocompatibility of NTCGM scaffolds was confirmed, their ability to induce terminal osteoblast differentiation of human Saos-2 cells *in vitro* was further investigated due to the critical role of osteoblasts in the regulation of calcification processes and bone maturation.[58] Osteocytes are terminally differentiated osteoblasts that constitute about 90% of the cells embedded within the bone matrix.[59] These cells play critical roles in controlling mineral homeostasis and bone formation and resorption,[60] by producing calcification-modifying hormones and growth factors[61] and altering the matrix around them.[62] During bone formation and maturation, alkaline phosphatase (ALP), the major enzyme in mineralization, is a known marker to determine the degree of development and function of differentiating osteoblasts. In our case, ALP activity was evaluated in Saos-2 cells cultured on NTC, NTCG and NTCGM scaffolds, as well as tissue culture plastic (TCP) as an additional control surface. Differentiation is typically promoted in the presence of osteogenic factors so that cells were incubated in calcifying media (ODMEM). Nonetheless, certain osteoblast differentiation can also occur in regular DMEM (*i.e.* absence of osteogenic factors) due to the natural maturation of an osteoblast culture in the presence of calcium ($CaCl_2$, 200 mg L^{-1}) and inorganic phosphates (NaH_2PO_4, 125 mg L^{-1}), both components of the normal formulation of DMEM. Thus, the non-calcifying media DMEM was also used as a control. After incubation in ODMEM, cells cultured on TCP experienced a significant increase in ALP activity. The incremental ratio of ALP activity from DMEM to ODMEM was 1.19 at 7 days (7.24 for ODMEM vs 6.10 for DMEM, units mg protein^{-1} cm^{-2}, see Table 3-SI) and increased 1.4-fold (to 1.68) after 14 days. The incremental ratios of ALP activity on NTC and NTCG scaffolds at 7 days were 0.84 and 0.97 and increased to 1.23 and 1.25 after 14 days, respectively (**Figure 10**). These numbers were slightly below those found on TCP. However, one should consider that we are providing data normalized by surface. In the scaffold case, this surface is the base of the cylinder (e.g. 0.16 cm^2), while the real surface on which cells are growing is just a fraction of that because of the presence of pores (see Figure 8 and 9). Actually, the increase of the incremental ratio of ALP activity from 7 to 14 days –which is not dependent on the neat surface area– was nearly the same as on TCP (ca. 1.4-fold).

Nonetheless, the most interesting data was found for NTCGM scaffolds. In this case, the incremental ratio of ALP activity at 7 days was 2.03, well above that found on TCP (Figure 10). Actually, the incremental ratio of ALP activity on NTCGM scaffolds was more than twice that on NTC and NTCG scaffolds at 7 days (ca. 2.03 versus 0.84-0.97, respectively) although similar values were finally found for all of them over time (ca. 1.2 at 14 days). The remarkable acceleration of osteoblast terminal differentiation observed for NTCGM scaffolds in just 7 days should be ascribed to the presence of DCPD. Actually, previous studies in bone regeneration have demonstrated that calcification drives osteocyte maturation.[63] For instance, the ALP activity of mouse preosteoblastic MC3T3-E1 cells cultured on HA-electrodeposited PLLA nanofibrous scaffolds exhibited a significant increase in the presence of osteogenic factors.[39] Moreover, a fully differentiated phenotype in human primary osteoblasts was obtained on a 3D culture system based on biphasic calcium phosphate ceramic particles (60% hydroxyapatite + 40% tricalcium phosphate, 40–80 μm in diameter) even in the absence of osteogenic factors.[64] The adsorptive properties of MWCNT have been also hypothesized as factors contributing to promote calcium deposition and enhance ALP activity. For instance, pegylated-MWCNT and graphene induced osteoblast differentiation of mesenchymal stem cells in the presence of osteogenic factors such

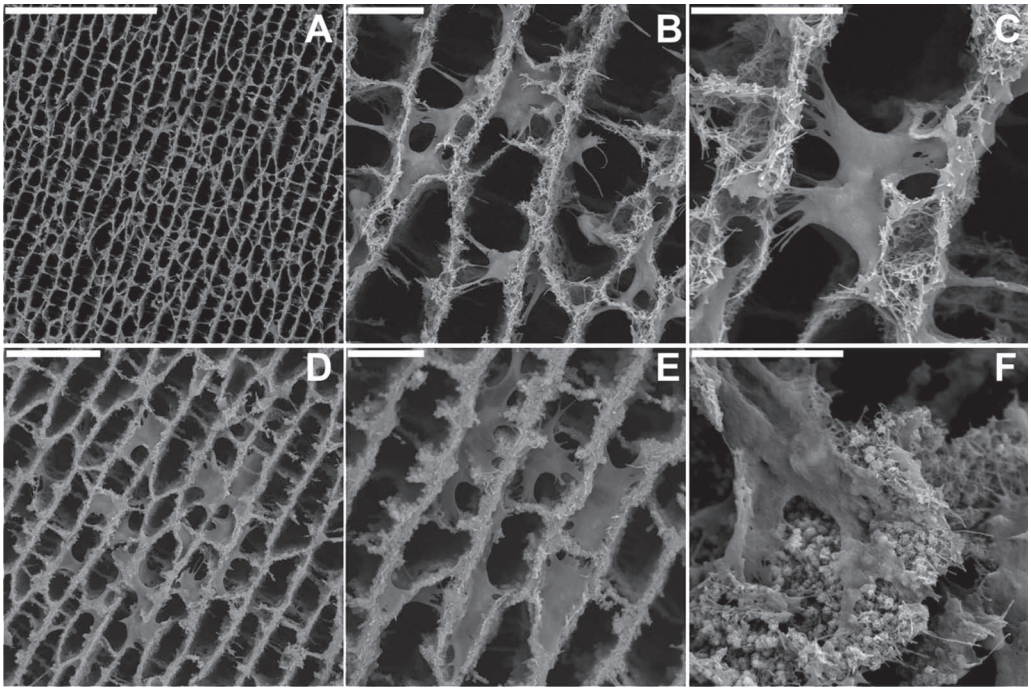

Figure 8. Representative SEM images of human Saos-2 osteoblasts cultured on NTC (A-C) and NTCGM scaffolds (D-F). As observed, cells attached and spread on the materials with a clear tendency to colonize the microchannels. Homogenous DCPD electrodeposition in NTCGM scaffolds was also confirmed (D, E). Cells adequately adhered on electrodeposited flower-like DCPD (F). Scale bars represent 200 μm (A), 50 μm (D) and 20 μm (B,C,E,F).

as ascorbic acid and β-glycerol phosphate.[65,66] Meanwhile, the decrease in ALP activity observed at 14 days could be ascribed to cell-related processes such as extracellular matrix formation and osteoblast culture maturation after confluence[67] that, as culture progresses, could acquire more relevant roles in the differentiation than at the early stages.

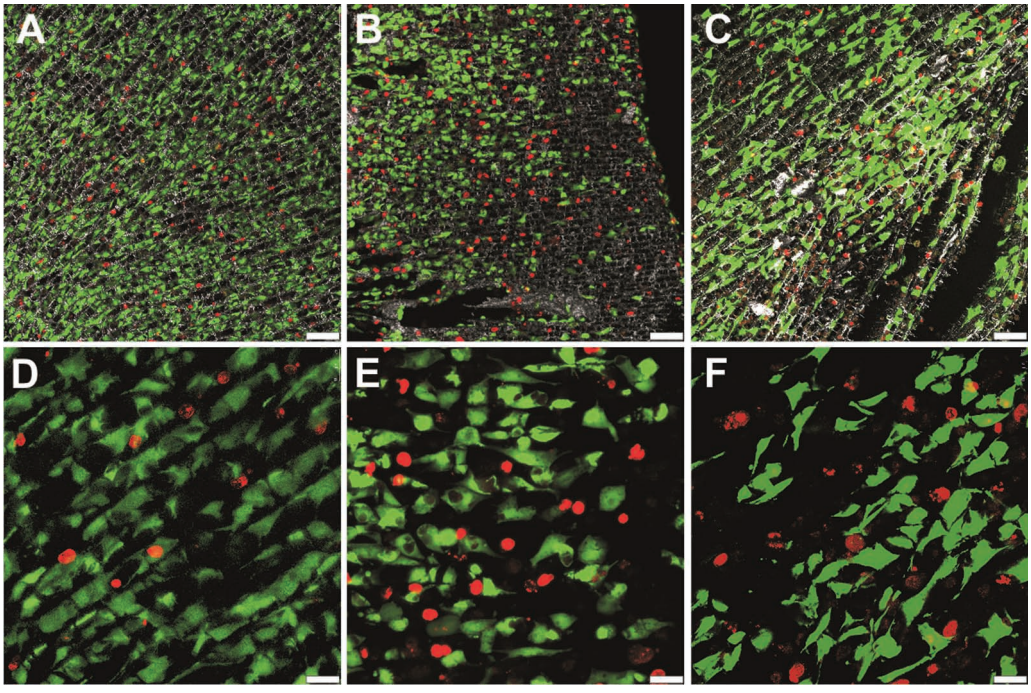

Figure 9. Cell viability studies of human Saos-2 osteoblasts cultured on NTC (A, D), NTCG (B, E) and NTCGM (C, F) scaffolds by CLSM. Representative images are shown. Scale bars represent 75 μm (A-C) and 25 μm (D-F).

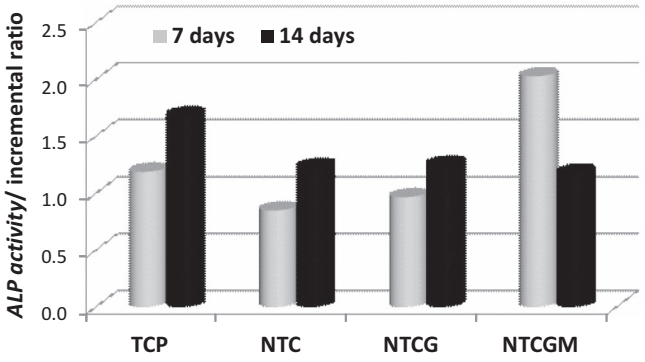

Figure 10. Incremental ratio of ALP activity (ODMEM versus DMEM) studied in human Saos-2 osteoblasts cultured on NTC, NTCG and NTCGM scaffolds.

3. Conclusions

In conclusion, we have applied a "flow-through" electrodeposition process for the homogeneous mineralization of the internal structure of "true" 3D scaffolds composed of chitosan and MWCNT. We demonstrated the validity of the mineralization process for electrodepositions carried out over different times and/or using different temperatures, voltages and even salt solutions (Figure 3-SI). Thus, we confirmed that the continuous feed of salts provided by the use of a flow-through configuration is the main issue if one desires to coat the entire internal structure of 3D scaffolds with a homogeneous mineral layer. These scaffolds showed a remarkable biocompatibility when tested with human osteoblast cells. Interestingly, the initial presence of DCPD on these materials promoted a faster and significant osteoblast terminal differentiation (as early as 7 days in calcifying media). We hypothesized that the osteoconductive properties of NTCGM scaffolds, along with the osteoinductive mediators that will be released by the surrounding injured bone tissue immediately after damage,[68] might be sufficient to successfully support bone healing in a more rapid fashion. Overall, these scaffolds could be considered as attractive multifunctional materials for bone healing and regeneration by combining a 3D hierarchical structure, biocompatibility and osteoconductive properties.

4. Experimental Section

Materials: Chemical reagents were purchased from Sigma-Aldrich and used as received unless otherwise indicated. For the preparation of the scaffolds, low molecular weight chitosan (CHI, Batch #06513AE, Brookfield viscosity 20000 cps), glutaraldehyde (50 wt% in distilled water) and multiwall carbon nanotubes (MWCNT, diameter 110-170 nm, length 5–9 μm) were used. Cell culture media and supplements were purchased from Lonza and used following manufacturer's indications.

Preparation of NTC Scaffolds: NTC scaffolds (where NT stands for multiwall carbon nanotube and C for chitosan) were prepared as described elsewhere.[45] Briefly, CHI solutions (1 wt%) were obtained by dissolving CHI (0.1 g) in an aqueous solution of acetic acid (10 g, 0.15 M, pH 4.5). MWCNT (1 g) were functionalized under reflux in nitric acid (50 mL, 14 M) at 130 °C for 5 h. After cooling, the functionalized-MWCNT were repeatedly washed with distilled water until complete nitric acid removal and then allowed to dry. Functionalized-MWCNT (300 mg) were then dispersed in a CHI solution (5 g, 1 wt%) by stirring at room temperature for 24 h and finally sonicated for 4 min. The MWCNT/CHI suspension was then collected into insulin syringes (1 mL) and dipped at a constant rate of 5.9 mm min^{-1} into a cold bath maintained at a constant temperature of –196 °C (liquid nitrogen). The unidirectionally frozen samples were freeze-dried using a thermoSavant Micromodulyo freeze-drier. The resulting monoliths kept both the shape and the size of the insulin syringes. Before mineralization, NTC scaffolds were additionally exposed to glutaraldehyde vapors at room temperature for 24 h for CHI crosslinking. The so obtained NTCG scaffolds (where G stands for glutaraldehyde) were subsequently aerated over further 24 h before use.

3D Electrode Preparation: The 3D electrode was produced from monolithic cylinders of 4.5 mm in diameter and 12.0 mm in height, as described elsewhere.[69] Briefly, the cylindrical scaffold was glued to a piece of carbon thread for electrical connection (using graphite adhesive 112 from Electron Microscopy Sciences) and then sealed (using shrink tubing and heating to 120 °C over 5 min) to a glass tube of similar diameter (Figure 2).

Electrodeposition: Electrodeposition was carried out using $Ca(NO_3)_2$ (20 mM) and $NH_4H_2PO_4$ (12 mM) in deionized water as electrolyte.[70,71] $NaNO_3$ (0.1 M) was also added to improve the ionic strength of the solution. The pH of the electrolyte was adjusted to 4.2 by the addition of hydrochloric acid. The dissolution was stirred using a magnetic bar over 2 h to ensure the complete dissolution of the calcium and phosphate salts. Finally, the solution was filtered through 0.45 μm syringe filters before use.

The electrochemical cell worked in both static (i.e. absence of flow) and flow-through configuration. In both cases, the electrolyte solution was forced to flow through the microchanneled structure of the NTCG scaffold using an Ismatec tubing pump. After impregnation of the scaffold internal structure, the flow was stopped and the scaffold was placed in the beaker filled with further electrolyte (10 mL). Finally, the scaffold was plugged to the current intensity supplier (a Voltalab PGZ301) through the carbon thread. No further manipulation than turning on the power supply was required to work in static conditions whereas in flow-through configuration, a continuous flow of electrolyte (0.250 mL min^{-1}) was also forced to diffuse through the microchanneled internal structure of the 3D electrode.

Electrodeposition was performed in a 10 mL beaker tightly sealed with a cap. The electrodeposition setup consisted of three electrodes: a platinum mesh (Goodfellow) electrode ($10 \times 10 \times 0.2$ mm^3) as the counter electrode (anode), the above-described assembly of NTCG scaffold as the working electrode (cathode) and an Ag/AgCl electrode (Bioanalytical systems) as reference. The three electrodes were placed into the beaker and then, immersed in a silicon bath at the temperature of choice. The resulting scaffold was abbreviated as NTCGM, where additional M stands for mineralized.

Scaffold Characterization: The morphology of non-mineralized and mineralized scaffolds (NTC, NTCG and NTCGM) was observed using a Zeiss DSM-950 scanning electron microscope (SEM). The morphology of the different crystals was also investigated in a 200-KeV JEOL JEM-2000FX electron transmission microscope (TEM). Selected area electron diffraction (SAED) was used to assess the crystallinity of the sample. Calibrated energy dispersion X-ray spectroscopy (EDS) was used to provide the Ca/P ratio of the different samples. XRD patterns were performed in a Bruker D8 Advance difractometer using the CuKα radiation (0.05° step size and 3.5 sec counting time).

Cell Culture: Cell cultures were performed on NTC, NTCG and NTCGM scaffolds of 4.5 mm in diameter and *ca.* 3 mm in height, obtained from the electrodeposited ones (4.5 mm in diameter and 12 mm in height) by cryo-fracture. Thus, every electrodeposited monolith provided up to four scaffolds for cell culture. The scaffolds were sterilized under UV radiation for 20 min per side and preconditioned in culture medium for 24 h to eliminate any toxic residues prior to cell culture. Human osteoblast-like Saos-2 cells were cultured at a density of 10^5 cells per scaffold in DMEM supplemented with fetal bovine serum (10%), streptomycin (100 UI ml^{-1}), penicillin (100 UI ml^{-1}), and L-glutamine (1 mM) under

a CO_2 (5%) atmosphere and at 37 °C. Tissue culture plastic (TCP) was used as a control surface in all experimental conditions.

Morphological Studies: Cells cultured over 2 days on the scaffolds were rinsed in PBS twice and fixed with glutaraldehyde solution in PBS (2.5%) for 45 min. After washing in distilled water, dehydration was performed by slow water replacement. Thus, the scaffolds were soaked in series of ethanol solutions (30%, 50%, 70%, and 90%) over 15 min (twice in every solution) and finally in absolute ethanol for 30 min. After drying at room temperature for 24 h, samples were mounted in stubs and coated with gold under vacuum. The cells cultured on the scaffolds were examined with a DSM-950 scanning electron microscope (Zeiss).

Viability Studies: The viability was assessed in cells cultured over 5 days on the different scaffolds by using a Live/Dead® Viability kit (Invitrogen) according to the manufacturer's instructions. After staining, samples were observed in a Leica SP5 confocal laser scanning microscope (CLSM). The fluorescence of both probes (i.e. calcein and ethidium homodimer-1) was excited by the 488 nm light of an Argon laser. After excitation, fluorescence emission was separated using a triple dicroic filter 488/561/633 and measured at 505–570 nm for green fluorescence (calcein) and 630–750 nm for red fluorescence (ethidium homodimer-1). Physical reflexion from the scaffolds after excitation at 488 nm was also recorded and used to observe the scaffold structure and the relative cellular location. Cell viability was provided as number of live (green) and dead (red) cells counted over at least 6 square fields randomly distributed in 20× confocal images.

Terminal Osteoblast Differentiation: Saos-2 cells were cultured at a density of 5×10^4 cells per scaffold in culture media (DMEM). After 5 days, cultures were either maintained in regular media or incubated in calcifying media (ODMEM) for 7 and 14 days. ODMEM consisted of DMEM supplemented with the following osteogenic factors: ascorbic acid (50 μg ml^{-1}), *β*-glycerol phosphate (10 mM) and dexamethasone (1 μM), well-known inducers of osteoblast differentiation.[72] Culture media was replaced every other day.

Alkaline Phosphatase Activity Studies: Alkaline phosphatase activity (ALP) was analyzed in cell cultures as described elsewhere.[72] Briefly, cell cultures were first rinsed with PBS twice to eliminate any residue from the culture media that might interfere with the assay. Then, cells were incubated with RIPA buffer for cell lysis, scraped from the plate wells and then collected in microcentrifuge tubes to finally be spinned down at 10,000 × *g* for 10 min. Supernatants were transferred to clean tubes and separated for both ALP assay and total protein content assay. For ALP evaluation, the conversion of *p*-nitrophenyl phosphate (pNPP) by the alkaline phosphatase present in the samples was monitored at 405 nm. Specifically, 10 μl of sample were added to 90 μl of pNPP (10 mM in 2-amino-2-methyl-1-propanol buffer 0.1 M containing $MgSO_4$ 2.3 mM) and the reaction followed by absorbance at 405 nm for 15 min at room temperature. Samples were run in duplicate and three different dilutions for each sample were carried out to guarantee detection in an acceptable range. Absorbance values obtained were converted to ALP activity in Units ml^{-1} and finally normalized by protein content (mg) and surface area (cm^2). Total protein content was measured by a standard MicroLowry assay, where bovine serum albumin was used for the preparation of the standard curve. Endothelial cells were used as negative control for ALP expression.

Statistics: Values were expressed as mean ± standard deviation. Statistical analysis was performed using the Statistical Package for the Social Sciences software (SPSS, version 17.0). Comparisons among three or more groups were done by analysis of variance (ANOVA), followed by Scheffé or Games-Howell *post hoc* tests after evaluation of variance homogeneity among groups. For comparisons between two groups, t Student test was performed. In all statistical evaluations, $p < 0.05$ was considered statistically significant.

Supporting Information

Supporting Information is available from the Wiley Online Library or from the author.

Acknowledgements

This work was supported by grants from MINECO (Project Numbers MAT2009-10214 and MAT2011-25329) and from the European Union Seventh Framework Programme (FP7/2007-2013) under grant agreement number 263289 (Green Nano Mesh). S.N. acknowledges CSIC for a *JAE-Pre* fellowship. M.C.S. is greatly in debt with MINECO for a Juan de la Cierva fellowship. Fernando Pinto (from the *Instituto de Ciencias Agrarias -CSIC*) and Sylvia Gutiérrez (from the *Centro Nacional de Biotecnología-CSIC*) are acknowledged for their assistance with SEM and confocal microscopy studies, respectively.

Received: March 13, 2012
Revised: May 17, 2012
Published online: June 20, 2012

[1] A. Praemer, S. Furner, D. P. Rice, *Musculoskeletal conditions in the United States*, 2nd ed., American Academy of Orthopaedic Surgeons, Park Ridge, IL, **1999**.
[2] N. E. Lane, *Am. J. Obstet. Gynecol.* **2006**, *194*, S3.
[3] P. V. Giannoudis, H. Dinopoulus, E. Tsiridis, *Injury Int. J. Care Injured* **2005**, *36*, 20.
[4] K. Rezwan, Q. Z. Chen, J. J. Blaker, A. R. Boccaccini, *Biomaterials* **2006**, *27*, 3413.
[5] Q. Fu, E. Saiz, M. N. Rahaman, A. P. Tomsia, *Mater. Sci. Eng. C* **2011**, *31*, 1245.
[6] H. Qiu, J. Yang, P. Kodali, J. Koh, G. A. Ameer, *Biomaterials* **2006**, *27*, 5845.
[7] M. Bohner, U. Gbureck, J. E. Barralet, *Biomaterials* **2005**, *26*, 6423.
[8] S. A. Clarke, P. Walsh, C. A. Maggs, F. Buchanan, *Biotechnol. Adv.* **2011**, *29*, 610.
[9] S. Mann, *Biomineralization: Principles and Concepts in Bioinorganic Materials Chemistry*, Oxford Chemistry Masters, Oxford, UK **2001**.
[10] S. Mann, *Biomimetic Materials Chemistry*, VCH Publishers, New York **1996**.
[11] F. C. Meldrum, H. Cölfen, *Chem. Rev.* **2008**, *108*, 4332.
[12] M. Antonietti, M. Breulmann, C. G. Göltner, H. Cölfen, K. K. W. Wong, D. Walsh, S. Mann, *Chem. Eur. J.* **1998**, *4*, 2493.
[13] N. A. J. M. Sommerdijk, G. de With, *Chem. Rev.* **2008**, *108*, 4499.
[14] G. Wang, L. Zheng, H. Zhao, J. Miao, C. Sun, H. Liu, Z. Huang, X. Yu, J. Wang, X. Tao, *ACS Appl. Mater. Interfaces* **2011**, *3*, 1692.
[15] H.-W. Kim, J.-H. Song, H.-E. Kim, *Adv. Funct. Mater.* **2005**, *15*, 1988.
[16] S.-H. Yu, H. Cölfen, M. Antonietti, *J. Phys. Chem. B* **2003**, *107*, 7396.
[17] S. Elhadj, E. A. Salter, A. Wierzbicki, J. J. De Yoreo, N. Han, P. M. Dove, *Cryst. Growth Des.* **2006**, *6*, 197.
[18] V. M. Rusu, C. Ng, M. Wilke, B. Tiersch, P. Fratzi, M. G. Peter, *Biomaterials* **2005**, *26*, 5414.
[19] B. M. Whited, J. R. Whitney, M. C. Hofmann, Y. Xu, M. N. Rylander, *Biomaterials* **2011**, *32*, 2294.
[20] H. R. Ramay, M. Zhang, *Biomaterials* **2003**, *24*, 3293.
[21] M. C. Gutiérrez, M. Jobbágy, M. L. Ferrer, F. del Monte, *Chem. Mater.* **2008**, *20*, 11.
[22] S. Deville, E. Saiz, K. Ravi, R. V. Nalla, A. P. Tomsia, *Science* **2006**, *311*, 515.
[23] J. S. Lee, D. Suarez-Gonzalez, W. L. Murphy, *Adv. Mater.* **2011**, *23*, 4279.
[24] D. Enlow, A. Rawal, M. Kanapathipillai, K. Schmidt-Rohr, S. Mallapragada, C.-T. Lo, P. Thiyagarajan, M. Akinc, *J. Mater. Chem.* **2007**, *17*, 1570.
[25] J. Song, V. Malathong, C. R. Bertozzi, *J. Am. Chem. Soc.* **2005**, *127*, 3366.

[26] S.-S. Kim, M. S. Park, O. Jeon, C. Y. Choi, B. S. Kim, *Biomaterials* **2006**, *27*, 1399.
[27] M. J. Hortigüela, M. C. Gutiérrez, I. Aranaz, M. Jobbágy, A. Abarrategi, C. Moreno-Vicente, A. Civantos, V. Ramos, J. L. López-Lacomba, M. L. Ferrer, F. del Monte, *J. Mater. Chem.* **2008**, *18*, 5933.
[28] S. Shanbhag, S. Wang, N. A. Kotov, *Small* **2005**, *1*, 1208.
[29] X. Lu, Y. Leng, Q. Zhang, *Surf. Coat. Technol.* **2008**, *202*, 3142.
[30] C. Wu, Z. Wen, C. Dai, Y. Lu, F. Yang, *Surf. Coat. Technol.* **2010**, *204*, 3336.
[31] S. Chen, W. Liu, Z. Huang, X. Liu, Q. Zhang, X. Lu, *Mater. Sci. Eng. C* **2009**, *29*, 108.
[32] A. Rakngarm, Y. Mutoh, *Mater. Sci. Eng. C* **2009**, *29*, 275.
[33] X. Cheng, M. Filiaggi, S. G. Roscoe, *Biomaterials* **2004**, *25*, 5395.
[34] A. Naldoni, A. Minguzzi, A. Vertova, V. Dal Santo, L. Borgese, C. L. Bianchi, *J. Mater. Chem.* **2011**, *21*, 400.
[35] A. O. Lobo, M. A. F. Corat, S. C. Ramos, J. T. Matsushima, A. E. C. Granato, C. Pacheco-Soares, E. J. Corat, *Langmuir* **2010**, *26*, 18308.
[36] N. Eliaz, S. Shmueli, I. Shur, D. Benayahu, D. Aronov, G. Rosenman, *Acta Biomater.* **2009**, *5*, 3178.
[37] J. Wang, Y. Chao, Q. Wan, Z. Zhu, H. Yu, *Acta Biomater.* **2009**, *5*, 1798.
[38] D. Richard, N. Dumelié, H. Benhayoune, S. Bouthors, C. Guillaume, N. Lalun, G. Balossier, D. J. Laurent-Maquin, *J. Biomed. Mater. Res. B: Applied Biomater.* **2006**, *79*, 108.
[39] C. He, G. Xiao, X. Jin, C. Sun, P. X. Ma, *Adv. Funct. Mater.* **2010**, *20*, 3568.
[40] M. C. Gutiérrez, M. L. Ferrer, F. del Monte, *Chem. Mater.* **2008**, *20*, 634.
[41] M. C. Gutiérrez, Z. Y. Garcia-Carvajal, M. Jobbagy, L. Yuste, F. Rojo, C. Abrusci, F. Catalina, M. L. Ferrer, F. del Monte, *Chem. Mater.* **2007**, *19*, 1968.
[42] Q. Shi, H. Liang, D. Feng, J. Wang, G. D. Stucky, *J. Am. Chem. Soc.* **2008**, *130*, 5034.
[43] Q. Shi, Z. An, C.-K. Tsung, H. Liang, N. Zheng, C. J. Hawke, G. D. Stucky, *Adv. Mater.* **2007**, *19*, 4539.
[44] J. L. Vickery, A. J. Patil, S. Mann, *Adv. Mater.* **2009**, *21*, 2180.
[45] M. C. Gutiérrez, Z. Y. Garcia-Carvajal, M. J. Hortigüela, J. Yuste, F. Rojo, M. L. Ferrer, F. del Monte, *J. Mater. Chem.* **2007**, *17*, 2992.
[46] N. Halonen, A. Rautio, A.-R. Leino, T. Kyllönen, G. Tóth, J. Lappalainen, K. Kordás, M. Huuhtanen, R. L. Keiski, A. Sápi, M. Szabó, A. Kukovecz, Z. Kónya, I. Kricsi, P. M. Ajayan, R. Vajtai, *ACS Nano* **2010**, *4*, 2003.
[47] J. Zou, J. Liu, A. S. Karakoti, A. Kumar, D. Joung, Q. Li, S. I. Khondaker, S. Seal, L. Zhai, *ACS Nano* **2010**, *4*, 7293.
[48] J. G. Duque, C. E. Hamilton, G. Gupta, S. A. Crooker, J. J. Crochet, A. Mohite, H. Htoon, K. A. D. Obrey, A. M. Dattelbaum, S. K. Doorn, *ACS Nano* **2011**, *5*, 6686.
[49] C. Lau, M. J. Cooney, *Langmuir* **2008**, *24*, 7004.
[50] M. C. Gutiérrez, M. J. Hortigüela, J. M. Amarilla, R. Jiménez, M. L. Ferrer, F. del Monte, *J. Phys. Chem. C* **2007**, *111*, 5557.
[51] A. Abarrategi, M. C. Gutiérrez, C. Moreno-Vicente, M. J. Hortigüela, V. Ramos, J. L. López-Lacomba, M. L. Ferrer, F. del Monte, *Biomaterials* **2008**, *29*, 94.
[52] S. R. Mukai, H. Nishihara, H. Tamon, *Chem. Commun.* **2004**, 874.
[53] H. Zhang, I. Hussain, M. Brust, M. F. Butler, S. P. Rannard, A. I. Cooper, *Nat. Mater.* **2005**, *4*, 787.
[54] S. Deville, E. Saiz, A. P. Tomsia, *Acta Mater.* **2007**, *55*, 1965.
[55] A. Bigi, E. Boanini, D. Walsh, S. Mann, *Angew. Chem. Int. Ed.* **2002**, *41*, 2163.
[56] Y.-H. Tseng, C.-Y. Mou, J. C. C. Chan, *J. Am. Chem. Soc.* **2006**, *128*, 6909.
[57] D. F. Williams, *Biomaterials* **2008**, *29*, 2941.
[58] S. L. Dallas, P. A. Veno, J. L. Rosser, C. Barragan-Adjemian, D. W. Rowe, I. Kalajzic, L. F. Bonewald, *Cells Tissues Organs* **2008**, *189*, 6.
[59] D. Zhu, N. C. W. Mackenzie, J. L. Millan, C. Farquharson, V. E. MacRae, *PLos One* **2011**, *6*, e19595.
[60] E. H. Burger, J. Klein-Nulen, *Adv. Dent. Res.* **1999**, *13*, 93.
[61] L. F. Bonewald, *Ann. N. Y. Acad. Sci.* **2007**, *1116*, 281.
[62] E. M. Aarden, P. J. Nijweide, A. van der Plas, M. J. Alblas, E. J. Mackie, M. A. Horton, M. H. Helfrich, *Bone* **1996**, *18*, 305.
[63] K. Irie, S. Ejiri, Y. Sakakura, T. Shibui, T. Yajima, *J. Histochem. Cytochem.* **2008**, *56*, 561.
[64] F. Boukhechba, T. Balaguer, J.-F. Michiels, K. Ackermann, D. Quincey, J.-M. Bouler, W. Pyerin, G. F. Carle, N. Rochet, *J. Bone Mineral Res.* **2009**, *24*, 1927.
[65] T. R. Nayak, L. Jian, L. C. Phua, H. K. Ho, Y. Ren, G. Pastorin, *ACS Nano* **2010**, *4*, 7717.
[66] T. R. Nayak, H. Andersen, V. S. Makam, C. Khaw, S. Bae, X. Xu, P.-L. R. Ee, J.-H. Ahn, B. H. Hong, G. Pastorin, B. Özyilmaz, *ACS Nano* **2011**, *5*, 4670.
[67] H. Siqqelkow, K. Benzler, M. J. Atkinson, M. Hüfner, *M. Exp. Clin. Endocrinol. Diabetes* **1998**, *106*, 217.
[68] T. Albrektsson, C. Johansson, *C. Eur. Spine J.* **2001**, *10*, S96.
[69] K. Katuri, M. L. Ferrer, M. C. Gutiérrez, R. Jiménez, F. del Monte, D. Leech, *Energy Environ. Sci.* **2011**, *4*, 4201.
[70] M. Shirkhanzadeh, *J. Mater. Sci.: Mat. Med.* **1998**, *9*, 67.
[71] M. Shirkhanzadeh, *J. Mater. Sci.: Mat. Med.* **1991**, *10*, 1415.
[72] L. A. Davis, A. Dienelt, N. I. zur Nieden, in *Methods in Molecular Biology*, (Ed: N. I. zur Nieden), Springer, *690*, **2011**, 255–272.